

<https://doi.org/10.1038/s41612-024-00681-7>

Crucial role of sea surface temperature warming patterns in near-term high-impact weather and climate projection

Check for updates

Ming Zhao & Thomas Knutson

Recent studies indicate that virtually all global climate models (GCMs) have had difficulty simulating sea surface temperature (SST) trend patterns over the past four decades. GCMs produce enhanced warming in the eastern Equatorial Pacific (EPAC) and Southern Ocean (SO) warming, while observations show intensified warming in the Indo-Pacific Warm Pool (IPWP) and slight cooling in the eastern EPAC and SO. Using Geophysical Fluid Dynamics Laboratory's latest higher resolution atmospheric model and coupled prediction system, we show the model biases in SST trend pattern have profound implications for near-term projections of high-impact storm statistics, including the frequency of atmospheric rivers (AR), tropical storms (TS) and mesoscale convection systems (MCS), as well as for hydrological and climate sensitivity. If the future SST warming pattern continues to resemble the observed pattern from the past few decades rather than the GCM simulated/predicted patterns, our results suggest (1) a drastically different future projection of high-impact storms and their associated hydroclimate changes, especially over the Western Hemisphere, (2) a stronger global hydrological sensitivity, and (3) substantially less global warming due to stronger negative feedback and lower climate sensitivity. The roles of SST trend patterns over the EPAC, IPWP, SO, and the North Atlantic tropical cyclone Main Development Region (AMDR) are isolated, quantified, and used to understand the simulated differences. Specifically, SST trend patterns in the EPAC and AMDR are crucial for modeled differences in AR and MCS frequency, while those in the IPWP and AMDR are essential for differences in TS frequency over the North Atlantic.

Global climate models (GCMs) are one of the most important tools for predicting future change in the Earth's climate under anthropogenic forcings. These models are not perfect and contain biases when evaluated against observations. Some biases may be more important than others. It is important to identify the key biases relevant to future predictions so that the modeling community can focus on improvements. Recent studies suggest that essentially all GCMs, including those with large ensemble (LE) simulations from varying initial conditions have had difficulty simulating the observed sea surface temperature (SST) trend patterns for the past few decades¹⁻³. In the historical simulations, GCMs generate intensified warming in the equatorial eastern Pacific along with Southern Ocean (SO) warming while the observations exhibit intensified warming in the Indo-Pacific Warm Pool (IPWP) and slight cooling in the eastern equatorial Pacific and Southern Ocean. The nature of such misrepresentation is still unclear and under debate²⁻¹⁰.

The latest GCMs from the Geophysical Fluid Dynamics Laboratory (GFDL) are no exception to these broad biases. For instance, in Fig. 1, we

present a comparison of several SST indices computed from the LE simulations of the historical period (1979-2020) using GFDL's Seamless System for Prediction and Earth System Research (SPEAR)¹¹ with the observational estimates based on the HadISST, ERSSTv5, COBE, and COBE2 dataset (see the Methods section for details). The SST indices include (1) a Pacific zonal east-west gradient (hereafter referred to as W-E index). (2) a poleward or equator off-equatorial gradient (hereafter referred to as O-E index). (3) a spatial pattern correlation in SST trends for the equatorial Pacific region as well as the entire global open ocean, (4) a ratio in SST trend between the IPWP and the entire tropical ocean, and (5) a ratio in SST trend between the SO and the entire global open ocean. (Refer to the Methods section for the definition of each index). Supplementary Fig. 1 shows the global distribution of the SST trend patterns from each individual member of the SPEAR LE as well as the observational estimates from the HadISST, ERSSTv5, COBE, and COBE2 dataset.

GFDL/NOAA, Princeton, New Jersey 08540, USA. ✉e-mail: Ming.Zhao@noaa.gov

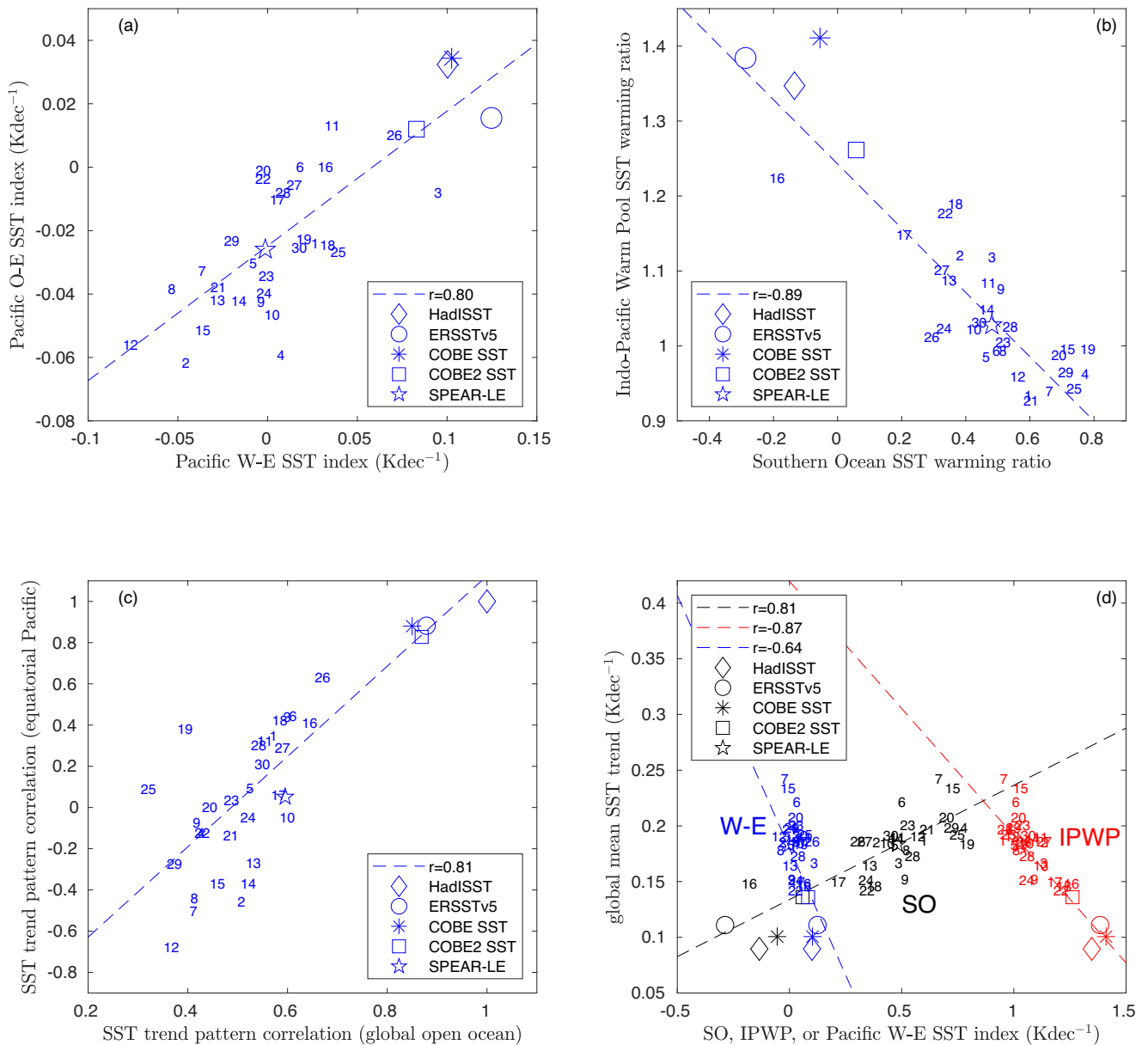


Fig. 1 | A comparison of SST trend pattern indices between SPEAR LE simulations and several observational estimates. a Scatter plot of the trends (K decade^{-1}) in Pacific equatorial east-west (W-E index) and equator off-equatorial SST gradient (O-E index) for the period of 1979–2020 from GFDL’s SPEAR LE simulations (numbers: individual members’ ID; pentagram: ensemble mean) and the observational estimates based on HadISST (diamond), ERSSTv5 (circle), COBE SST (asterisk), and COBE2 (square) SST dataset. **b** As in (a) but for the ratio of SST trends between the Indo-Pacific Warm Pool and the entire tropical ocean and that between the Southern Ocean and the global open ocean. **c** As in (a) but for the spatial pattern

correlation in SST trends between the model simulations (or an alternative observational data) and the HadISST data for the Pacific equatorial region and that for the entire global open ocean. **d** Scatter plots of the global open ocean area-weighted mean SST trend and the different SST indices shown in panel (a, b), i.e., (black) the SO warming ratio, (red) the IPWP warming ratio, and (blue) the Pacific equatorial east-west SST gradient. Linear regression lines and their corresponding correlation coefficient between various indices are shown in the legend. See Methods Section for the definitions of each SST index.

Figure 1a shows that except member 3 (members 11 and 26) all individual members of the SPEAR LE underestimate the trend of equatorial Pacific east-west (poleward) SST gradient, indicating that the model produces excessive equatorial eastern Pacific SST warming relative to the western Pacific and to the off-equatorial eastern Pacific. Choosing a narrower equatorial region such as 3°S – 3°N makes the model bias even worse. The model’s biases in the east-west and poleward gradients are generally correlated among the SPEAR members and the observational estimates, indicating they may be originated from the same process. Figure 1b further shows that none of the individual members of SPEAR LE reproduces the observed ratio in SST trend between IPWP and the tropical ocean mean SST. Moreover, except for one (member 16) all members produce excessive

relative warming of the SO. The underestimation of the IPWP warming and overestimation of the SO warming are also long-standing biases among the CMIP models¹ and they appear to be strongly correlated among the SPEAR ensemble members and the observational estimates. It turns out that the SST trend biases in IPWP and SO are also correlated to the Pacific equatorial east-west gradient despite with somewhat smaller correlation coefficients (0.65 for IPWP, 0.58 for SO). This suggests potentially a global scale coherence of the model’s systematic biases in SST trend patterns. Figure 1c shows a scatter plot of the pattern correlation coefficient between the SST trends from the model’s simulations (or alternative observations) and that from the HadISST data for the equatorial Pacific region and for the entire global open ocean. None of the individual members of SPEAR LE reproduce

the pattern correlation coefficients between alternative observations and the HadISST data. In particular, the SPEAR LE mean SST trend pattern shows little correlation with the HadISST data over the equatorial Pacific region. Despite its systematically lower correlation coefficients, the SST trend pattern correlation over the equatorial Pacific region is generally correlated with that over the global ocean among the SPEAR members and the observational estimates.

Finally, Fig. 1d shows that the global mean SST warming rate is strongly positively (negatively) correlated with the relative warming over the SO (IPWP) among the individual members of SPEAR LE and different observational data. Model members with less SO warming and more IPWP warming (e.g., member 16) are more consistent with the observations. The global mean SST warming rate across SPEAR LE is also negatively correlated with the equatorial Pacific east-west SST gradient despite with somewhat weaker correlation coefficient. This result is generally consistent with the notion that SST warming patterns are important to climate feedback and climate sensitivity^{12–16}. However, all individual members tend to overestimate the global mean SST warming rate. In particular, the global open ocean mean SST warming trend averaged from the SPEAR LE is $0.18 \text{ K decade}^{-1}$, which is about twice as large as that estimated based on the HadISST data ($0.09 \text{ K decade}^{-1}$). In general, Fig. 1 demonstrates that similar to other GCMs, GFDL's latest climate models have also trouble reproducing the observed SST trend patterns for the past 42 years, for which global observations of SSTs are most reliable. The various indices for measuring model biases in SST trend patterns over different ocean basins are significantly correlated. This indicates that the SST warming patterns in SPEAR LE generally follow some global-scale coherent variability that is spatially correlated and can strongly affect the global mean SST trend. Moreover, the observational estimates appear to sit beyond the far tail of the SPEAR ensemble spread. Figure 1 along with several recent studies^{1–3} raises the question of how seriously one should take this systematic model bias in terms of future climate prediction.

The primary focus of this study is to explore the implications of model biases in the recent SST trend pattern on near-term future predictions, with a special emphasis on high-impact storm statistics. We will also assess their impact on hydrological and climate sensitivity, both of which are essential factors for future climate projections. To achieve this, we utilize GFDL's high-resolution global atmospheric model AM4 (C192AM4), which is the same atmospheric model used in the SPEAR LE simulations. See the "Methods" section for details. This model has been demonstrated to realistically simulate the climatological frequency of atmospheric rivers (ARs), tropical storms (TSs), and mesoscale convective systems (MCSs), as well as their associated precipitation when it is forced by the observed SSTs, sea-ice concentrations, radiative gases and aerosol emissions^{17–20}. We first conducted three 101-year-long simulations, which include a present-day control simulation and two warmer climate simulations. In the warmer climate simulations, the patterns of SST trends for the 1979–2020 period are extrapolated into the future with the same global mean warming. The observed-pattern simulation uses the observed trend from the HadISST data, while the SPEAR pattern simulation uses the trend simulated by the 30-member ensemble mean (referred to as SPEAR-pattern M) of the SPEAR model. To explore the impact of the internal variability of the SPEAR LE, we conducted five additional simulations (SPEAR-patterns A–E) based on the performance of individual SPEAR members in simulating the observed Pacific equatorial zonal SST gradient. Furthermore, to isolate and explore the effects of the various regional differences in SST trend patterns between SPEAR-pattern M and the observed-pattern, we conducted four further simulations. These simulations mirror SPEAR-pattern M, except for replacing the SST anomalies in the Equatorial Pacific (EPAC), the IPWP, the SO, or the Atlantic tropical cyclone Main Development Region (AMDR) with those from the observed-pattern. Please refer to the Methods section for a detailed description of the simulations.

While the SPEAR-pattern M is entirely consistent with its future simulation/projection (not shown), our decision to extrapolate the observed pattern is not intended to offer a more realistic future projection. Instead, it

merely serves as a hypothesis for studying the consequences if the model-observational discrepancy persists into future decades. The actual future SST warming pattern may fall between the scenarios we explored here, including those of the various SPEAR patterns and the observed-pattern. To that extent, the extrapolation of observed SST trend pattern would provide an upper bound to estimate the impact of the models' systematic biases in future high-impact weather and climate prediction. Below, we demonstrate that the disparity between the modeled and observed SST warming patterns will have a profound impact on future predictions of regional changes in high-impact storms, global and regional hydrological cycle, as well as the global mean warming rate in response to greenhouse gas (GHG) increase.

Results

Impact of SST warming patterns on high-impact storms and hydrological cycle

ARs, TSs, and MCSs are important weather phenomena that often threaten society through heavy precipitation and strong winds. Ref. 19 shows that despite their rare occurrence, ARs, TSs, and MCSs together account for roughly 55% of global mean precipitation and 75% of extreme precipitation with daily rates exceeding its local 99th percentile. Before delving into the impact of SST warming patterns on these high-impact storms, Fig. 2a, b first compares the spatial patterns of the SST warming anomalies from the two different future climate simulations. Compared to the observed-pattern, SPEAR-pattern M exhibits more relative warming (or less relative cooling) in the tropical eastern Pacific and much muted relative warming over the IPWP. The tropical Pacific east-west SST gradient is broadly weakened in the SPEAR-pattern M rather than strengthened as in the observed-pattern. Interestingly, the strengthening of the east-west SST gradient in the observed-pattern, compared to the SPEAR-pattern M, can also be discerned in the equatorial Indian Ocean and the North Atlantic tropical cyclone main development region, albeit with a much weaker magnitude. In addition, the SPEAR-pattern M also displays much less relative SST cooling over the broad southern oceans than the observed-pattern apart from the SW Pacific ($0\text{--}30^\circ\text{S}$), which shows relative warming in observations. Figure 2c–h shows the geographical distribution of the model-simulated changes in the occurrence frequency of AR, TS, and MCS days (see "Methods" section for the detection of AR, TS, and MCS days) from the SPEAR-pattern M and the observed-pattern of warmer climate simulations. They reveal striking differences especially over the western hemisphere. For example, the observed-pattern produces a much larger reduction in the frequency of AR days over the northeastern Pacific, much of the continental US, as well as the subtropical to middle latitudes of the South American continent. For TS days, the observed-pattern produces a strong reduction in the subtropical central to eastern North Pacific and a large increase in the Gulf of Mexico, Caribbean Sea, and the west coast of Mexico while the SPEAR-pattern M produces an increase in the subtropical central North Pacific, a small reduction near the west coast of Mexico, a very mild increase in the Gulf of Mexico, but a substantial increase in the broad North Atlantic. Globally, the frequency of TS days decreases by $11\% \text{K}^{-1}$ ($-0.075/0.68$) in the observed-pattern simulation while increases slightly ($0.6\% \text{K}^{-1}$, $0.004/0.68$) in the SPEAR-pattern M simulation. For MCS days, the observed-pattern produces a large reduction over the continental US and tropical central to eastern Pacific while the SPEAR-pattern M yields a much smaller reduction in the continental US and an increase in the equatorial northeastern Pacific. These results indicate the importance of SST warming patterns to future projections of high-impact storm statistics. In particular, if the future change in SST warming patterns (including near-term changes from the next decade to the next half century) continue to follow the observed pattern from the past 42 years instead of that simulated or predicted by the current climate models, we may experience a very different future occurrence frequency of these high-impact storms than the current climate model projections, especially over the US and its surrounding Pacific and Atlantic oceans.

To demonstrate the impact of SST warming patterns on future changes in hydroclimate, Fig. 3 compares the model simulated changes in the

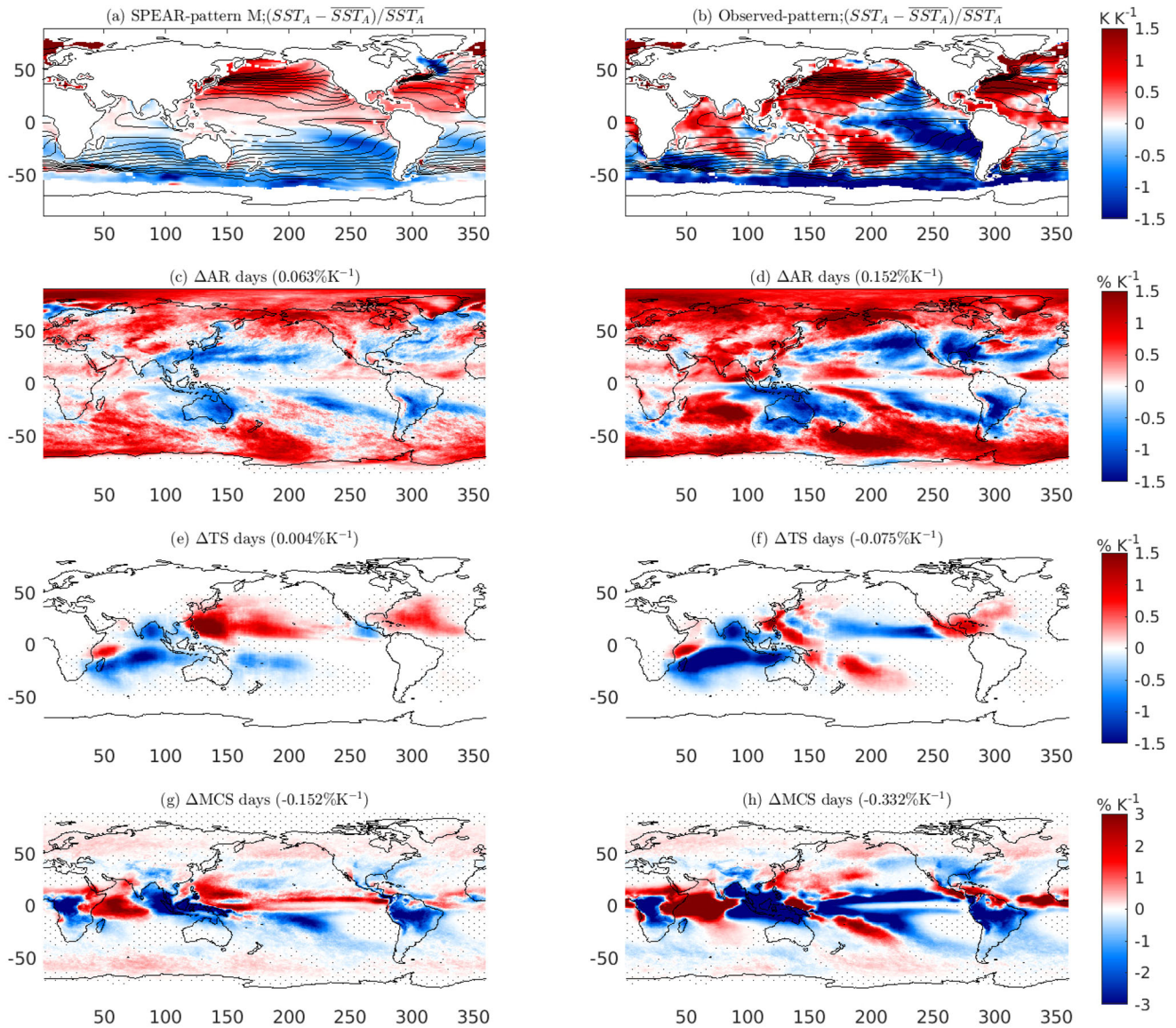


Fig. 2 | SST warming patterns and their impact on model-simulated atmospheric river (AR), tropical storm (TS), and mesoscale convective system (MCS) frequencies are compared between simulations based on the SPEAR-pattern M and the observed pattern of SST trends. a, b SST warming anomalies [shown as normalized values i.e., $(SST_A - \overline{SST}_A)/\overline{SST}_A$ (shading), overbar denotes global open ocean area-weighted mean] derived from the SST trend of (a) the 30-member ensemble mean of SPEAR LE simulations and (b) the HadISST dataset for the period of 1979–2020. $\overline{SST}_A = 0.92$ K in both warmer climate simulations (see “Methods” section for details). The black contours in panels (a, b) show the observed climatological distribution of annual mean SSTs (280–302 K with a contour interval of 2K)

from the model’s control simulation. **c, d** Geographical distribution of model-simulated changes in the occurrence frequency of AR days, normalized by the change in global mean surface air temperature (unit: $\%K^{-1}$) from (c) SPEAR-pattern M and (d) Observed-pattern warmer climate simulations. **e, f** As in (c, d) but for TS days. **g, h** As in (c, d) but for MCS days. The change in global area-weighted mean frequency is shown on the top of panels (c–h). The global frequency of AR, TS and MCS days from the control simulation is respectively 7.71%, 0.68%, and 4.92%. Stippled areas in panels (c–h) indicate regions where the changes are not statistically significant at a 95% confidence level based on z-test.

geographical distribution of annual mean precipitation rate and its contribution from changes in AR, TS, and MCS days. The global mean change is shown on the top of each panel. The SPEAR-pattern M and observed-pattern simulations result in an increase of $0.092 \text{ mm day}^{-1} K^{-1}$ ($3.13\%K^{-1}$) and $0.124 \text{ mm day}^{-1} K^{-1}$ ($4.22\%K^{-1}$) in global mean precipitation, respectively. These numbers are significantly larger than those obtained from typical coupled simulations²¹. This is primarily because we did not change the radiative gases in the warmer climate simulation, allowing us to focus specifically on the impact of SST warming. Compared to the SPEAR-pattern M, the observed-pattern produces roughly 35% [i.e., $(0.124 - 0.092)/0.092$] larger increase in global mean precipitation, indicating a substantially stronger global hydrological sensitivity to warming. Regionally, the observed-pattern produces a large reduction in annual precipitation over

much of the eastern Pacific, the US, and the South American continent and a large increase in the Gulf of Mexico and the Caribbean Sea while the SPEAR-pattern M produces a substantial increase in the equatorial eastern Pacific, little change in the US, and only a modest increase over the Gulf of Mexico and the Caribbean Sea. At the ocean basin scale, the observed-pattern tends to produce broad westward shifts in precipitation in the tropical Pacific and the tropical Indian Ocean with an enhanced large-scale zonal Walker circulation. For example, Fig. 3b displays a substantial increase in precipitation in the equatorial western Pacific east of the maritime continent, which extends southeastward along the South Pacific Convergence Zone (SPCZ) and a decrease to the east. Similarly, it also shows a large increase (decrease) in precipitation in the equatorial western (eastern) Indian Ocean. Although the precipitation change over the Indian Ocean is qualitatively similar

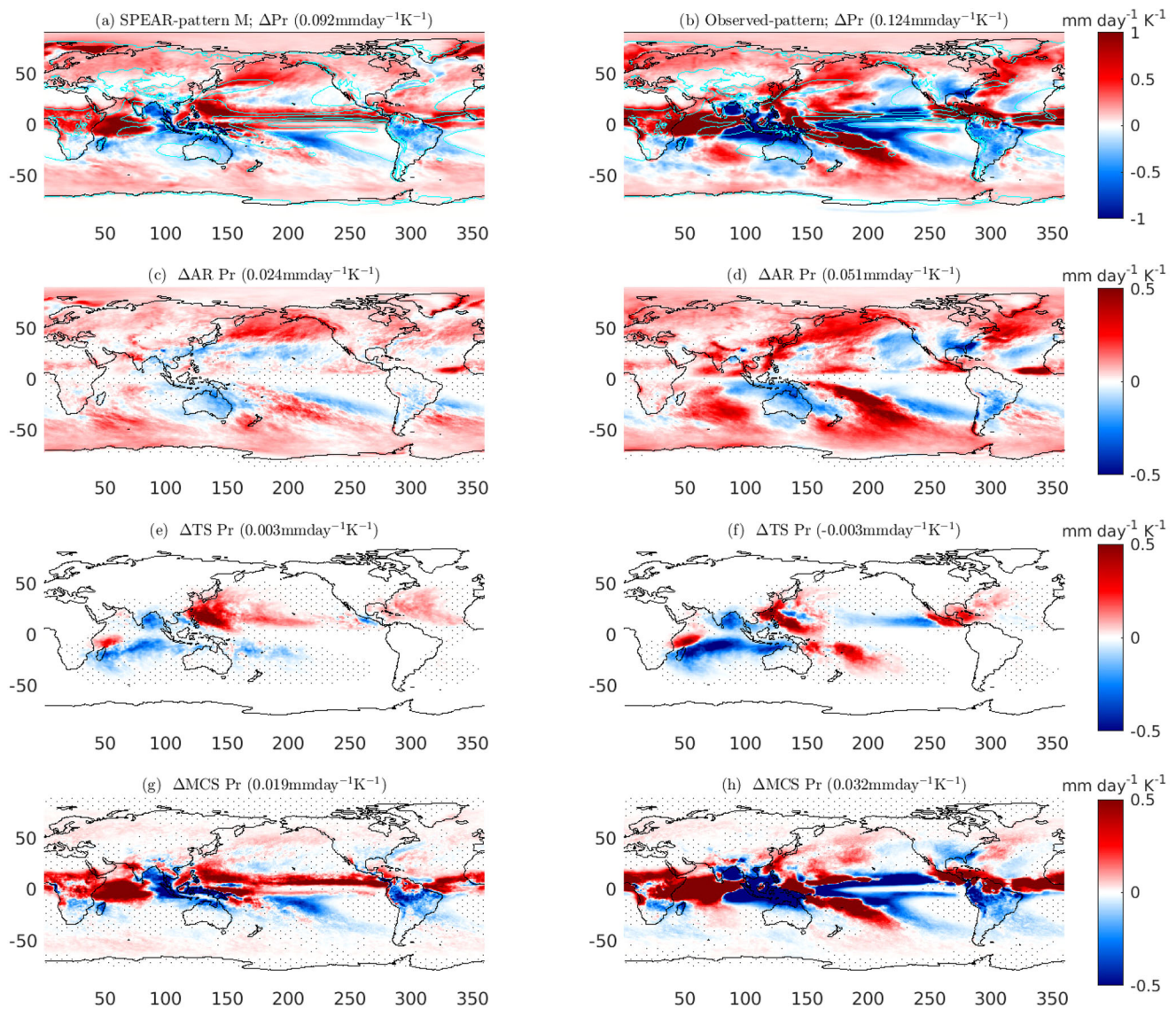


Fig. 3 | A comparison of simulated annual mean and storm-associated precipitation changes based on SST changes using the SPEAR-pattern M versus the observed pattern. a, b Geographical distribution of model-simulated changes in annual mean precipitation rate (shading, unit: $\text{mm day}^{-1} \text{K}^{-1}$), normalized by the change in global mean surface air temperature from (a) SPEAR-pattern M and (b) Observed-pattern warmer climate simulations. The cyan contours in panels a,b display isolines (1, 5, and 9 mm day^{-1}) of the climatological annual mean

precipitation simulated from the model's control simulation. **c, d** As in (a, b) but for AR-associated precipitation change. **e, f** As in (a, b) but for TS-associated precipitation change. **g, h** As in (a, b) but for MCS-associated precipitation change. The global area-weighted mean value is shown on the top of each panel. Stippled areas in panels (c, h) indicate regions where the changes are not statistically significant at a 95% confidence level based on z-test.

between the observed-pattern and SPEAR-pattern M simulations, the observed-pattern generates much stronger zonal dipole structure in precipitation change than the SPEAR-pattern M. Over the subtropical North Atlantic, the observed-pattern simulation exhibits a substantially stronger increase in precipitation over the Caribbean Sea and the Gulf of Mexico, with a more significant reduction to the east compared to the SPEAR-pattern M simulation.

The change in global mean and regional distribution of precipitation between the two different SST warming pattern simulations can be decomposed into precipitation changes associated with AR, TS, and MCS days, as well as other daily weather regimes. Compared to the SPEAR-pattern M simulation, the enhanced global hydrological cycle in the observed-pattern simulation is due entirely to precipitation change associated with storms. In particular, the global mean precipitation response to warming increases by $0.032 \text{ mm day}^{-1} \text{K}^{-1}$ (from 0.092 to $0.124 \text{ mm day}^{-1} \text{K}^{-1}$) while the global storm-associated (AR, TS, and MCS

together) precipitation increase by $0.034 \text{ mm day}^{-1} \text{K}^{-1}$ (from 0.046 to $0.08 \text{ mm day}^{-1} \text{K}^{-1}$). The enhanced response in global mean precipitation and associated latent heating is nearly entirely balanced by an increase in the response of atmospheric radiative cooling rate (the response in surface sensible heat flux remains relatively unchanged), which is in turn caused by the strengthening of tropical large-scale convective overturning motion and associated changes in weather regimes around the globe. Figure 3 further shows that the large reduction in US precipitation in the observed-pattern simulation is due primarily to the reduction in AR- and MCS-associated precipitation while the large reduction in the equatorial eastern Pacific (increase in precipitation in the Gulf of Mexico, Caribbean Sea, and the west coast of Mexico) is caused by the reduction (increase) in MCS- and TS-associated precipitation (comparing Fig. 3a, b with Fig. 3c–h). Note changes in storm-associated precipitation depend on changes in both storm frequency and their precipitation intensity with the former usually dominating the spatial variation of the total change¹⁹. In general, the difference in the

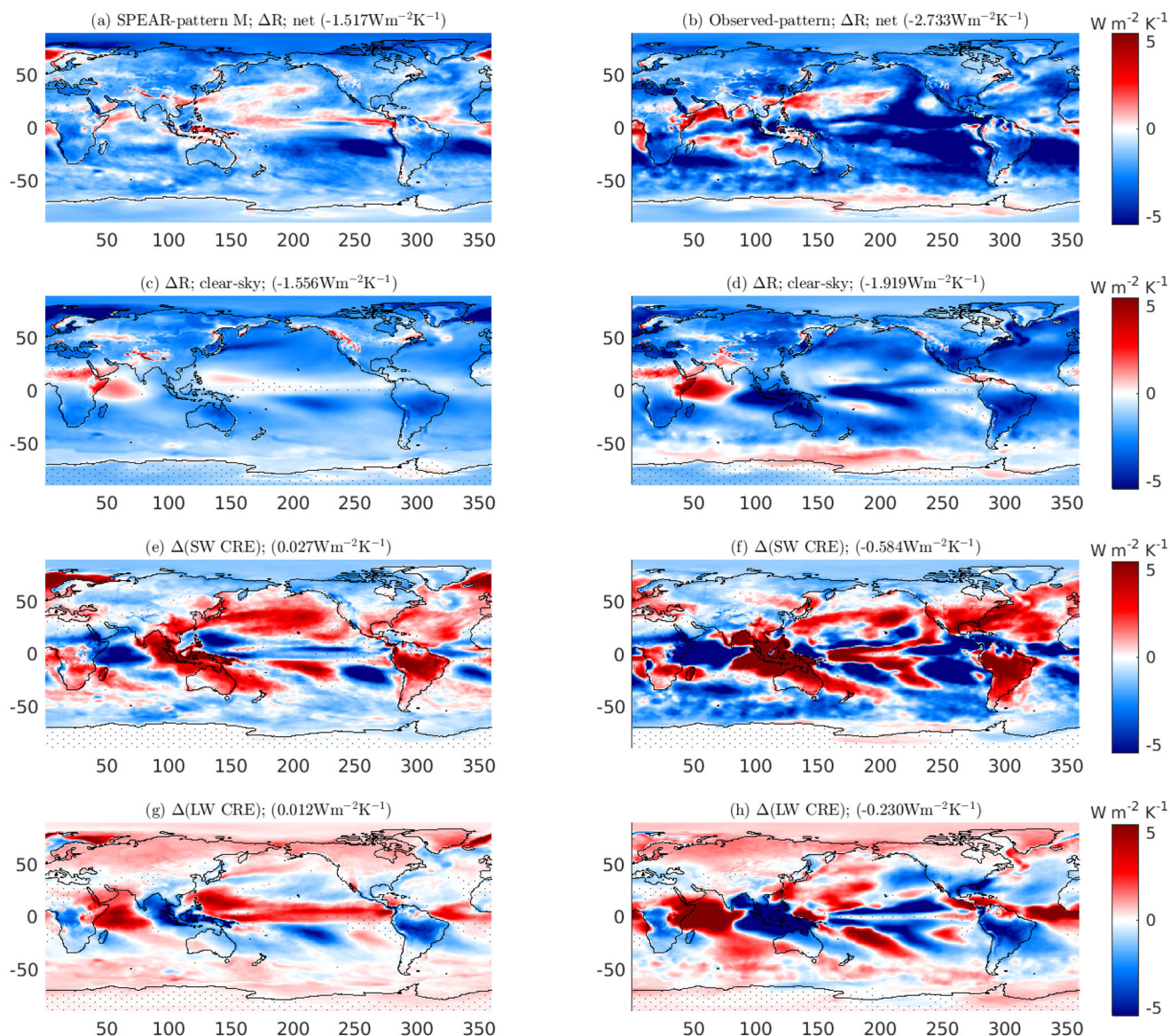


Fig. 4 | A comparison of simulated TOA net radiative feedback and its decomposition into clear-sky, LW, and SW cloud feedback based on SST changes using the SPEAR-pattern M versus the observed pattern. a, b Geographical distribution of model-simulated TOA net radiative feedback (unit: $W m^{-2} K^{-1}$) from (a) SPEAR-pattern M and (b) Observed-pattern warmer climate simulations. **c, d** As in (a, b) but for TOA clear-sky radiative feedback. **e, f** As in (a, b) but for TOA SW cloud feedback

measured by changes in SW cloud radiative effect (CRE) per degree global mean surface air temperature (SAT) warming. **g, h** As in (e, f) but for TOA LW cloud feedback measured by changes in LW CRE per degree global mean SAT warming. The global area-weighted mean value is shown on the top of each panel. Stippled areas in panels (c–h) indicate regions where the changes are not statistically significant at a 95% confidence level based on z-test.

global mean and regional distribution of annual precipitation between the two different warmer climate simulations can be well understood through the storm-associated precipitation with the AR-associated precipitation dominating the middle latitudes, MCS-associated precipitation dominating the deep tropics, and TS-associated precipitation contributing significantly in the subtropics.

Impact of SST warming patterns on climate feedback and climate sensitivity

The differences in SST warming patterns have a profound impact on not only regional changes in high-impact storms, global and regional hydrological cycles, but also the model’s climate feedback and climate sensitivity. Figure 4a, b compares the model simulated change in top-of-atmosphere (TOA) net radiative flux from the SPEAR-pattern M and the observed-pattern SST warming pattern simulations. While the SPEAR-pattern M produces a global negative feedback of roughly $-1.52 W m^{-2} K^{-1}$, the

observed-pattern yields a negative feedback ($-2.73 W m^{-2} K^{-1}$), which is nearly 80% larger in magnitude, indicating much less warming for the same GHG radiative forcing at the TOA. This suggests that if SPEAR LE produced the correct SST trend pattern for the past few decades, the model would produce a much reduced global mean warming rate, which would be more consistent with the HadISST observation. This is also important for future climate projection because if the future warming pattern continues to follow the observed pattern from the past few decades, it would suggest much less future global mean warming than that projected by the model for a given GHG and aerosol emission scenario.

Figure 4c, d further shows that among the additional $-1.21 W m^{-2} K^{-1}$ global feedback from the observed pattern simulation, roughly 30% ($-0.36 W m^{-2} K^{-1}$) comes from the clear-sky and 70% ($-0.85 W m^{-2} K^{-1}$) from the cloud feedback, in which ~50% ($-0.61 W m^{-2} K^{-1}$) is due to shortwave (SW) feedback and 20% ($-0.24 W m^{-2} K^{-1}$) is due to longwave (LW) feedback. Regionally, most of the increase in negative feedback comes

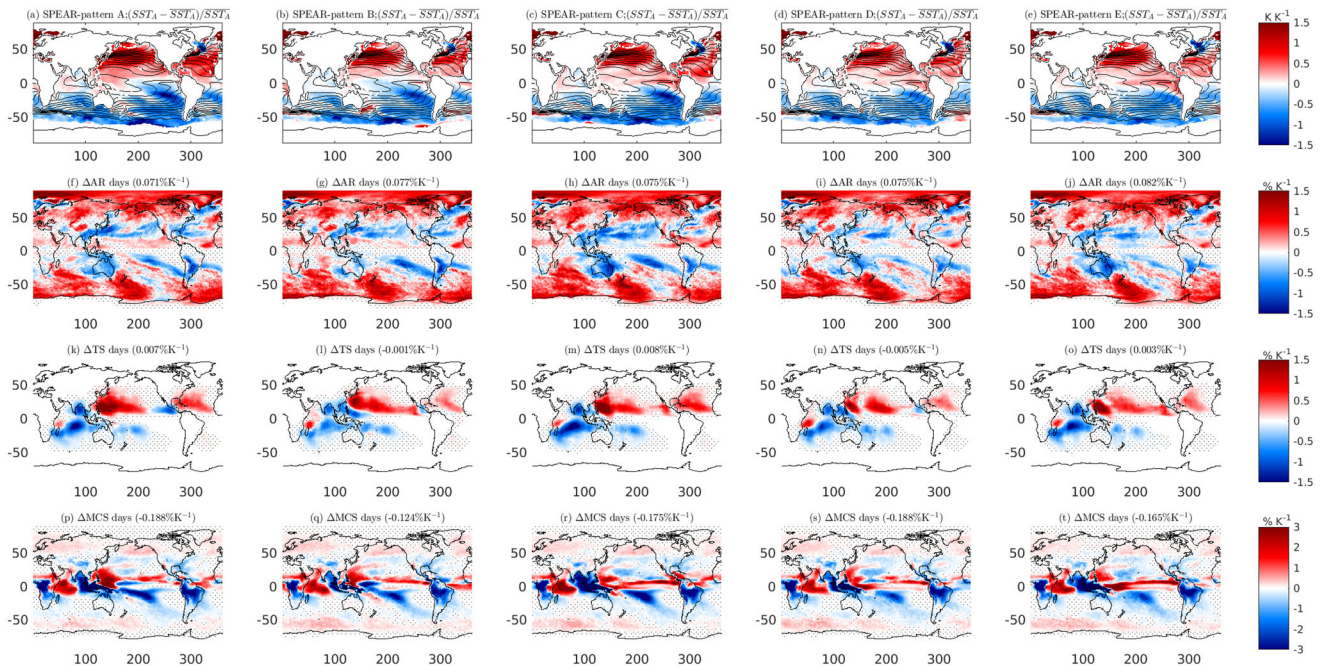


Fig. 5 | A comparison of SST warming patterns and model-simulated storm frequency changes for the SPEAR-pattern A to E simulations. As in Fig. 2, but for (from left to right columns) SPEAR-pattern A, B, C, D, and E simulations. The top

row (a–e) displays the SST warming patterns, while the second to fourth rows show the simulated changes in the occurrence frequency of AR (f–j), TS (k–o), and MCS (p–t) days, respectively.

from the eastern Pacific and southern oceans, which is due primarily to an increase in low cloud cover. Much of the regional changes in TOA radiative fluxes in the tropics are directly related to changes in convection and associated precipitation which affect spatial distribution of water vapor and clouds. For example, compared to the SPEAR-pattern M, the increase (less negative) in SW and decrease (less positive) in LW cloud radiative effect (CRE), as well as the more negative clear-sky feedback in the central to eastern equatorial Pacific is due to a reduction in convection and precipitation (see Fig. 3a, b), which are in turn caused by the relative cooling in SSTs over this region. In contrast, the increase in convection and precipitation over the east of the maritime continent and the off-equatorial regions of the western Pacific including those along the SPCZ lead to a decrease (more negative) in SW and an increase (more positive) in LW CRE there. Similarly, over the Indian Ocean, the strengthening of zonal dipole structure in changes in SW and LW CRE is also caused by a reduction in convection over the eastern Indian Ocean and maritime continent and an increase in convection over the western Indian Ocean (see Fig. 3a, b, g, h). The changes in spatial distribution of moist convection and precipitation in response to the different SST warming patterns also affect TOA radiative fluxes over the remote subsidence regions (e.g., eastern Pacific) by changing low clouds and clear-sky OLR through changes in tropospheric static stability and moisture^{22–25}. Globally, this may account for the majority of the enhanced negative feedback in the observed-pattern simulation compared to the SPEAR-pattern M simulation. Finally, local SST cooling over the broad eastern Pacific and the middle to high latitude oceans of the southern hemisphere also appear to contribute substantially to the more negative SW cloud feedback in the observed-pattern compared to the SPEAR-pattern M simulation.

Sensitivity to internal variability of SST trend patterns in SPEAR LE

So far, we have explored the impact of SST warming patterns on the global distributions of high-impact storm statistics and surface precipitation, as well as TOA radiative feedback between the SPEAR-pattern M and the observed-pattern simulations. However, the SPEAR-pattern M represents the SST trend pattern averaged from the SPEAR LE, while the observed-

pattern comes from a single realization containing both forced signals and internal variability. Ideally, conducting a simulation for each of the 30 members would provide the most comprehensive assessment, but this would demand a large amount of computational resources. Therefore, as an initial exploration of the role of internal variability within SPEAR LE in explaining the modeled differences between the SPEAR-pattern M and observed-pattern simulations, we conducted five additional simulations. These simulations, referred to as SPEAR-patterns A, B, C, D, and E, were based on the performance of individual SPEAR members in simulating the observed equatorial Pacific zonal SST gradient, with A denoting the best-performing and E the worst-performing group (see the Methods section for a detailed description of the experiments).

Figure 5 demonstrates that, compared to SPEAR-pattern M, SPEAR-pattern A shows only slightly better agreement with the simulation using the observed SST pattern. For instance, compared to SPEAR-pattern M, SPEAR-pattern A produces a greater reduction in AR frequency over the northeastern Pacific near the west coast of the US and in the central and southeastern US. It also generates a greater reduction in TS frequency and a lesser increase in MCS frequency in parts of the eastern Pacific. However, these differences are generally much smaller than their differences with the observed-pattern simulation. The model-simulated changes in AR, TS, and MCS frequency in SPEAR-patterns A to E simulations remain very similar to those in the SPEAR-pattern M simulation when compared to the simulation using the observed SST pattern. Supplementary Figs. 4 and 5, respectively show the simulated changes in surface precipitation and TOA radiative fluxes from the simulations of SPEAR-patterns A to E. These results further confirm that the essential differences between the SPEAR-pattern M and the observed-pattern simulations exist across the SPEAR-patterns A to E simulations, indicating they likely arise primarily from the model’s systematic biases in SST trend patterns.

Roles of regional SST trend patterns

To explore the key aspects of the differences in SST warming patterns between SPEAR-pattern M and the observed-pattern that may cause the simulated differences in changes in AR, TS, and MCS frequency, as well as the global distribution of surface precipitation and TOA radiative feedback,

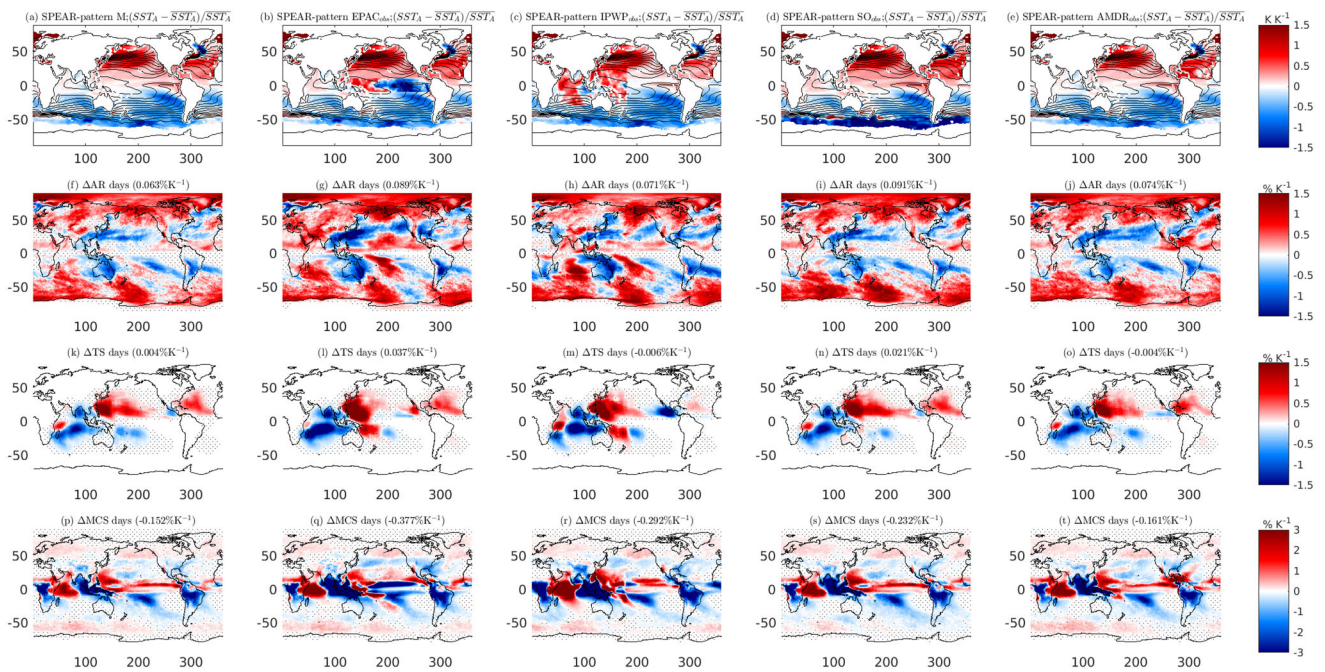


Fig. 6 | A comparison of SST warming patterns and model-simulated storm frequency changes between the SPEAR-pattern M and various modified SPEAR-pattern M simulations. As in Fig. 2, but for (from left to right columns) the SPEAR-pattern M, $EPAC_{obs}$, $IPWP_{obs}$, SO_{obs} and $AMDR_{obs}$ simulations. The top row (a–e)

displays the SST warming patterns, while the second to fourth rows show the simulated changes in the occurrence frequency of AR (f–j), TS (k–o), and MCS (p–t) days, respectively. The results from SPEAR-pattern M are reproduced in the left column for easier comparison with the rest of the simulations.

we carried out four more simulations. These simulations are the same as the SPEAR-pattern M, except for replacing the SST anomalies in the Equatorial Pacific, the IPWP, the SO, and the AMDR with those from the observed-pattern. (The SSTs outside of the replaced region may undergo minor changes due to the rescaling of the global open ocean mean SST to the same value. They are referred to as SPEAR-patterns $EPAC_{obs}$, $IPWP_{obs}$, SO_{obs} , $AMDR_{obs}$, respectively; see the Methods section for a detailed description of the simulations.) Figure 6 shows that, compared to SPEAR-pattern M, the SPEAR-pattern $EPAC_{obs}$ simulation produces a large reduction in AR frequency over the northeastern Pacific along with the west coast of the US, the central and eastern US, and Australia, making it substantially more similar to that in the observed-pattern simulation, particularly over the North America continent, Australia, and their surrounding oceans. It also enhances the AR frequency over parts of the northern high latitudes, such as Alaska, the Bering Sea, and the part of Russia close to the Bering Sea. This simulation also results in a substantial reduction in MCS frequency in the central to eastern Pacific, the North and South America continents, further aligning it with that of the observed-pattern simulation. However, its impact on TS frequency appears relatively small, except over the southwest Pacific and the west coast of Mexico. In contrast, the SPEAR-pattern $IPWP_{obs}$ produces a large reduction in TS frequency in both the broad North Atlantic and the eastern Pacific tropical cyclone main development region (MDR), aligning the TS frequency change over these regions more closely with the observed-pattern simulation. The SST anomalies in neither of these two regions can account for the increase in TS frequency in the Caribbean Sea and Gulf of Mexico in the observed-pattern simulation. It turns out that this can be explained by the SPEAR-pattern $AMDR_{obs}$ simulation. The enhanced (reduced) warming over the western (eastern) portion of the Atlantic tropical cyclone MDR in SPEAR-pattern $AMDR_{obs}$ tends to produce a westward shift of TS frequency and thus strong increase in TS frequency over the Caribbean Sea and Gulf of Mexico. In addition, compared to the SPEAR-pattern M and the observed-pattern simulations, the SPEAR-pattern $AMDR_{obs}$ significantly contributes to the reduction in AR frequency in the US, the northeastern Pacific, and the east coast of the US. Furthermore, it also contributes to the increase in MCS frequency in the

Caribbean Sea, the west coast of Mexico, and parts of the Gulf of Mexico. Thus, the SST trend patterns in the equatorial Pacific, the IPWP, and the North Atlantic tropical cyclone MDR region are all important for future projections of AR, TS, and MCS frequency, although their roles differ in different regions and for different types of storms. Finally, the model-simulated changes in storm frequency in the SPEAR-pattern SO_{obs} simulation look very similar to SPEAR-pattern M, except for AR frequency over the southern high latitude ocean and TS frequency over the southwest Pacific near Australia. This suggests that the difference in SO SST trends between the SPEAR-pattern M and the observed-pattern has a minimum direct impact on storm frequency over remote regions.

Supplementary Fig. 6 shows both total and individual storm-associated surface precipitation from the SPEAR-pattern $EPAC_{obs}$, $IPWP_{obs}$, SO_{obs} and $AMDR_{obs}$ simulations. Consistent with its simulated changes in AR and MCS frequency, the SPEAR-pattern $EPAC_{obs}$ produces AR- and MCS-associated precipitation changes more closely aligned with the observed-pattern simulation. This includes a drying trend for AR-associated precipitation over the northeastern Pacific near the west coast of US, the central and eastern US, and Australia, and a wetting trend over the central North and South Pacific ocean around 200°E longitude. Additionally, there is a large drying trend for MCS-associated precipitation in the tropical central and eastern Pacific. These changes together make its pattern in total precipitation change more similar to that from the observe-pattern simulation. However, the SPEAR-pattern $EPAC_{obs}$ does not help to explain the difference in TS-associated precipitation between SPEAR-pattern M and the observed-pattern simulations, particularly over the eastern Pacific and North Atlantic. In contrast, the SPEAR-pattern $IPWP_{obs}$ contributes to the muted increase in TS-associated precipitation in much of the North Atlantic, as well as the reduction in TS-associated precipitation over the eastern Pacific tropical cyclone MDR region. Neither the SPEAR-pattern $EPAC_{obs}$ nor the SPEAR-pattern $IPWP_{obs}$ account for the increase in TS-associated precipitation over the Caribbean Sea and Gulf of Mexico, which can be accounted for through the SPEAR-pattern $AMDR_{obs}$ simulation. Additionally, the SPEAR-pattern $AMDR_{obs}$ also explains the increase in MCS precipitation over the Caribbean Sea and the west coast of Central

America in the observed-pattern simulation. Finally, compared to the rest of the simulations, SPEAR-pattern EPAC_{obs} appears to play a dominant role in the increase of the global hydrological cycle from the SPEAR-pattern M to the observed-pattern simulation.

Supplementary Fig. 7 further displays the TOA radiative feedback from the SPEAR-pattern EPAC_{obs}, IPWP_{obs}, SO_{obs}, and AMDR_{obs} simulations. Compared to SPEAR-pattern M, SPEAR-pattern EPAC_{obs} explains most of the simulated differences in the patterns of clear-sky, LW and SW cloud feedback particularly over the central to eastern Pacific. All three components exhibit more negative or less positive feedback in response to the warming pattern, aligning the response closer to that in the observed-pattern simulation. Despite this, globally, only 43% of the increase in the magnitude of the negative feedback between SPEAR-pattern M and the observed-pattern is explained by the SPEAR-pattern EPAC_{obs} simulation. This indicates that SST trends over other regions also play an important role in the difference in global feedback strength between the SPEAR-pattern M and observed-pattern simulations. Indeed, the SPEAR-pattern IPWP_{obs} simulation also generates more negative feedback for all three components, and together they also amount for roughly 40% of the total increase in the magnitude of the negative feedback between the SPEAR-pattern M and observed-pattern simulations. Regionally, the SPEAR-pattern IPWP_{obs} tends to provide a better explanation for TOA radiative feedback over the Indian Ocean and West Pacific sector, particularly the enhanced zonal dipole structure between the equatorial eastern Indian Ocean and the equatorial western Indian Ocean and the Maritime Continent.

Compared to the SPEAR-patterns EPAC_{obs} and IPWP_{obs}, the SPEAR-pattern SO_{obs} and AMDR_{obs} simulations contribute only 13% and 4%, respectively, to the increase in the magnitude of global negative feedback from SPEAR-pattern M to the observed-pattern simulations, indicating their relatively small direct impact on global radiative feedback in this model. However, it is worth noting that although the SPEAR-pattern EPAC_{obs} and IPWP_{obs} simulations appear to reasonably describe both the spatial distribution of the feedback and the global increase in the magnitude of total negative feedback, they do not appear to explain the global change in SW cloud feedback well. For example, the SPEAR-patterns EPAC_{obs} and IPWP_{obs} account for only 19% and 29%, respectively, of the decrease (more negative) in SW cloud feedback from the SPEAR-pattern M to the observed-pattern simulation. This indicates that local SST cooling trend over large areas of the off-equatorial eastern Pacific and South Atlantic oceans (not accounted for by any of the experiments) may also contribute substantially to the enhanced negative SW cloud feedback.

Discussion

Recent studies suggest that GCMs have had trouble simulating the observed SST trend patterns for the past few decades for which global observations of SSTs are most reliable. We have investigated the GFDL SPEAR LE simulations of the historical period and found similar biases even considering the modeled internal variability. The biases are spatially correlated indicating global coherence of the systematic errors. Furthermore, we have explored the potential impact of the model's biases in future climate predictions, with a particular emphasis on high-impact storm statistics such as the frequency of AR-, TS-, MCS-days, their associated regional changes in precipitation, as well as the global hydrological and climate sensitivity.

Since all current GCMs are performing poorly in simulating SST trend patterns, we do not attempt to provide a best guess of future SST warming patterns. Instead, we choose to simply extrapolate the modeled and observed SST trends into future decades. This serves as our first step to explore the possible impact of the different SST warming patterns on a range of socially important questions. While the extrapolation of SPEAR's SST trend into the future is indeed consistent with the model's simulation/projection of future decades, it remains unknown how the actual SST warming pattern will unfold in the coming decades, and it may fall somewhere between the idealized scenarios explored here. To that extent, our results may provide a rough upper bound for estimating the impact of the models' systematic biases on near-term climate projections. Our results indicate that if the

future SST trend pattern continues to resemble the observed pattern from the past few decades rather than that simulated or predicted by climate models, we would anticipate a drastically different picture of future changes of high-impact storm statistics, especially the frequency occurrence of ARs, TSs, and MCSs over the Western Hemisphere, a stronger global hydrological sensitivity to warming, and substantially less global mean warming due to stronger negative feedback and lower climate sensitivity. Each of these is crucial for informative future climate projections. While we have not conducted simulations with SST trend patterns derived from each of the 30 members of SPEAR LE, which would provide the most comprehensive assessment, additional simulations with SST trend patterns derived from the five groups ranging from the best to the worst performance in simulating the equatorial zonal SST gradient show that the differences in future predictions persist across the spectrum, indicating that these differences likely stem primarily from the model's systematic errors in SST trend patterns.

To understand the simulated differences, we further conducted a series of simulations to isolate and quantify the effects of several key regional differences in SST trend patterns between the model and the observations. These simulations reveal the various roles of SST trend pattern contributions over the EPAC, IPWP, SO, as well as AMDR. The model biases in SST trend in both the EPAC and the AMDR (i.e., a trend of weakening instead of strengthening of the east-west SST gradient) are important factors causing the simulated differences in AR frequency, particularly in the US and its surrounding oceans. Moreover, the former is also important for the modeled differences in MCS frequency in the eastern Pacific, while the latter is important for MCS frequency in the Caribbean Sea, the Gulf of Mexico, and the west coast of Mexico. However, the model bias in the EPAC does not appear to explain well the simulated differences in TS frequency, particularly in the eastern Pacific and North Atlantic sector. In contrast, the SST trend pattern in IPWP and AMDR together can explain these differences well. In particular, compared to the SPEAR modeled SST warming pattern, the enhanced relative warming over the IPWP in the observations tends to suppress TS frequency over the entire North Atlantic and eastern Pacific. Meanwhile, the enhanced relative warming over the Caribbean Sea and relative cooling over the eastern portion of the AMDR tend to shift North Atlantic TS towards the Caribbean Sea, the Gulf of Mexico, and the west coast of Mexico. Compared to other regions, the model bias in SST trend pattern over the SO has a minimal direct impact on storm frequency, particularly over the remote regions. These regional differences in SST trend pattern account for not only the model-simulated differences in storm frequency but also for their associated precipitation, changes in the geographical distribution of annual climatological precipitation, as well as the strengthened global hydrological cycle in the observed-pattern simulation. Finally, the SST trend patterns in the EPAC and IPWP each contribute roughly 40% of the difference in global radiative feedback between the model (i.e., SPEAR-pattern M) and observed pattern simulations, indicating that both are important to global climate feedback. However, they only account for respectively 19% and 29% of the difference in SW cloud feedback, suggesting that local SST cooling over the broad off-equatorial eastern Pacific and southern hemisphere middle to high latitude oceans are also important to the enhanced negative SW cloud feedback in the observed-pattern simulation. Given the enormous impact of model biases in these regional SST trend patterns, it is essential to understand the origins of these biases before we can make more accurate future projections. Our result is consistent with a recent study that discussed the potential impact of coupled Earth System Model biases on near-term tropical cyclone risk²⁶. In addition, our study explored an expanded set of key drivers of extreme precipitation events in response to the SST warming patterns. This has only become possible recently due to our advancements in high-resolution atmospheric modeling, which not only enables reasonable representations of ARs, TSs, and MCSs but also allows for simulations long enough (100 years) to study changes in extreme storm statistics under various climate change scenarios^{17–20}.

While the global hydrological sensitivity does not directly impact local communities, it has been a theoretical concern in climate science for a long

time. Notably, its connections to global climate sensitivity, as revealed here, are of particular interest. Previous studies suggest that climate models tend to simultaneously produce overly strong climate sensitivity but weaker hydrological sensitivity^{27–30}. Ref. 30 hypothesizes that a missing iris effect in the models might be a possible cause of their muted hydrological change and higher climate sensitivity. The hypothesis suggests that the dry and clear regions of the tropical atmosphere might expand in a warmer climate and thereby allow more infrared radiation to escape to space, resulting in less warming and stronger hydrological sensitivity. This potential feedback has been termed the iris effect, in analogy to the enlargement of the eye's iris as its pupil contracts under the influence of more light³¹. The iris effect was often hypothesized and explored by assumptions of a particular change in the inherent property of convection in response to warming³⁰. Here, our results suggest an iris-like effect can be achieved through changes in large-scale SST warming patterns. However, the nature of this iris-like effect differs significantly from the original hypothesis because much of the enhanced outgoing radiation occurs through SW cloud reflection (Fig. 4e, f), as a result of an increase in low cloud cover in the subsidence regions (e.g., tropical eastern Pacific). The increase in low clouds also contributes to the increase in global total vertically-integrated atmospheric radiative cooling rate by emitting additional downward LW radiation to the surface. This, in turn, helps to amplify the global hydrological sensitivity.

Our results further indicate that the higher climate sensitivity and muted hydrological sensitivity in current GCMs may be caused by their inability to simulate the observed SST warming pattern for the past few decades. Indeed, the models tend to produce excessive warming in the eastern Pacific and the SO while the observations show intensified warming in the IPWP. When the observed SST warming pattern is imposed on our model, the enhanced warming over the IPWP, which contains the highest SSTs already, tends to lead to more convection aggregation over the warmest part of the oceans and suppress deep convection elsewhere. Hence, the model has the capacity to induce an iris-like effect by reorganizing convection and associated weather events spatially and temporally in response to shifts in SST warming patterns. Our results are broadly consistent with recent studies, which utilized highly idealized experiments to demonstrate that climate models' hydrological and climate sensitivities could be altered by changing the locations of SST warming or radiative forcing in the models^{32–38}.

While this study demonstrates the paramount importance of GCMs' ability in simulating and predicting SST trend patterns, it is beyond the scope of the present paper to explore the underlying causes of the models' systematic errors, especially over the equatorial Pacific. Recent studies have pointed to various directions, which is often confused by the different periods and regions used to estimate the trend of the SST gradient. For example, in ref. 2, the authors calculated the 60-year trends in Niño3.4 SST from 1958 to multiple ending years ranging from 2008 to 2017. They discovered a prominent model bias in all the periods ending in these years, with the later ending years showing larger biases. Furthermore, they argued that this bias is a result of the models' errors in response to the increase in GHG, which, in turn, stem from the models' cold climatological SST biases in the equatorial cold tongue region. However, in ref. 39, a different group of authors opted for a different time period (1950–2010) and considered somewhat different regions when calculating the Pacific zonal SST gradient. They concluded that the observed change in this gradient could be attributed to the models' internal variability. Ref. 1 focuses on the period from 1979 to 2020, expanding the SST indices to include measures not only of the Pacific equatorial SST gradient but also of the IPWP and Southern Ocean. The study found that the models' biases cannot be explained solely by the models' internal variability, especially when considering all the different bias indices together. Our analysis of the various indices for SST trend patterns simulated by the SPEAR LE shows that the observational estimates generally align with the regression lines of the SPEAR LE results. Thus, the observed SST trend pattern seems to agree with the coherence

of the SPEAR LE but falls beyond the models' ensemble spread, suggesting an underestimation of decadal internal climate variability in the model.

In addition to the potential model biases in internal variability and the forced response to GHG, other mechanisms and hypotheses have been suggested to explain the GCMs' inability to accurately simulate the recent SST trend pattern. For example, ref. 5–7,9 suggests that the Pacific equatorial SST trend error may arise in part from the absence of realistic Antarctic ice-sheet meltwater in climate models. Ref. 8,40,41 shows that the model bias may be affected by the models' representation of SO heat uptake. Both suggest the remote impact of the SO on the equatorial Pacific SST gradient. On the other hand, ref. 42 indicates that the recent unprecedented multiyear La Niña events may be attributed to the warming in the western Pacific. Despite recent research, it remains unclear to what extent the models' bias may be attributed to: deficiencies in representing internal variability; the forced response to changes in GHG and/or other climate forcing agents such as aerosols or ozone; the models' omission of important processes; or a combination of different factors. We propose that coordinated multi-model intercomparison experiments, testing various hypotheses along with mechanism denial experiments, could provide a valuable avenue for the modeling community to make progress on these issues.

Methods

Observations

We use several observational estimates of SSTs for comparison with the SPEAR LE simulations. They include the Hadley Centre Sea Ice and Sea Surface Temperature data set (HadISST, <https://www.metoffice.gov.uk/hadobs/hadisst/>), the NOAA Extended Reconstructed SST Version 5 (ERSSTv5, <https://psl.noaa.gov/data/gridded/data.noaa.ersst.v5.html>), the COBE (<https://psl.noaa.gov/data/gridded/data.cobe.html>), and COBE2 (<https://psl.noaa.gov/data/gridded/data.cobe2.html>) SST dataset.

Definition of SST indices

In this study, we employed five different SST indices to assess the differences between observations and model simulations in the SST trend pattern. These indices include (1) a zonal east-west gradient, referred to as the W-E index and defined as the trend in SST difference between a western Pacific box (110°–180°E, 10°S–10°N) and an eastern Pacific box (180°–280°E, 10°S–10°N), (2) a poleward or equator off-equatorial gradient, referred to as O-E index and defined as the trend in SST difference between the average of off-equatorial boxes for latitudes 10°–5°S and 5°–10°N and an equatorial box for latitude 5°S–5°N, all for longitudes 180°–280°E, (3) a spatial pattern correlation in SST trends between a model's simulation (or an alternative observational estimate) and the HadISST dataset for the equatorial Pacific region (110°–280°E, 10°S–10°N) as well as the entire global open ocean, (4) a ratio in SST trend between the IPWP (30°S–30°N, 50°–180°E) and the entire tropical ocean (30°S–30°N), and 5) a ratio in SST trend between the SO (45°–75°S) and the entire global open ocean. The first three indices are defined similarly as ref. 3 except with generally a larger region for each defined box. The fourth and fifth indices are similar to those in ref. 1 except with the SO index defined as a ratio to global open ocean mean instead of the absolute SO SST warming trend. The details in the definition of each index do not affect the results and conclusion qualitatively.

Models

The model we utilized here is a higher resolution version of the GFDL global atmospheric model AM4^{43,44}. It has been referred to as C192AM4¹⁷. C192AM4 employs a cubed-sphere topology for the atmospheric dynamical core with 192 × 192 grid-boxes per cube face corresponding to roughly ~ 50 km horizontal grid spacing. C192AM4 has been used for GFDL's participation in the CMIP6 High Resolution Model Intercomparison Project (HighResMIP)⁴⁵. C192AM4 has also been used for studies of ARs¹⁷, TSs⁴⁶, and MCSs¹⁸, as well as their associated precipitation and extreme precipitation¹⁹. In addition to C192AM4, we also used the SST simulations from the SPEAR model¹¹. SPEAR is the GFDL newly developed

coupled seasonal to multi-decadal prediction system consisting of AM4-LM4 atmosphere and land model, the MOM6 ocean and the SIS2 sea-ice model⁴⁷. SPEAR can be configured with three different atmospheric resolutions [i.e., low (100 km), medium (50 km), and high (25 km)]. The particular version of SPEAR we used here is the medium resolution (SPEAR-med), which uses C192AM4 as its atmospheric model.

Simulations

For this study, we conducted three 101-year-long simulations using C192AM4. The first is a Control simulation (referred to as Control) with the model forced by the observed monthly varying present-day climatological (1980–2014 average) SSTs, sea ice concentrations (SICs) from the HadISST dataset, and with the radiative gases, aerosol emissions, and solar constant fixed at the year 2010 condition. This kind of climatological run has long been used in GFDL's global atmospheric model development and it usually corresponds well to the model's present-day long-term climatology forced by interannual varying SSTs, SICs, radiative gases, and aerosol emissions. In addition to the Control simulation, we conducted two different warmer climate simulations, which are identical to the Control except by adding future SST warming anomalies to the HadISST climatological SSTs. We hypothesized two different scenarios for SST warming to create the SST anomalies. The first scenario, referred to as the SPEAR-pattern M (with M denoting ensemble mean), assumes that the 1979–2020 annual mean SST trend pattern from the ensemble mean of SPEAR LE will continue for the next 50 years (i.e., SST trends in K decade⁻¹ from panel e of Supplementary Fig. 1 multiplied by 5). The global open ocean mean SST anomaly is 0.92 K. The second scenario, referred to as the observed-pattern, assumes that the observed 1979–2020 annual mean SST trend pattern will continue for the next 50 years (i.e., SST trends from panel a of Supplementary Fig. 1 multiplied by 5). As we emphasize the impact of differences in SST warming patterns rather than the magnitude of global mean SST warming, we rescaled the SST anomalies from the observed pattern by multiplying them by a constant to ensure that the global open ocean mean SST anomaly matches that of the SPEAR-pattern M SST anomalies. Note that the seasonal variation in SST trend patterns in both SPEAR simulation and observations is generally small (see Supplementary Figs. 2, 3). Therefore, for simplicity, we do not consider the seasonal variation of the added SST anomalies. Note that the difference between the warmer climate simulations and the Control lies solely in their SSTs; there are no changes in the prescribed radiative gases and aerosol emissions. The monthly varying SSTs are simply repeated annually for 101 years, resulting in no interannual variability or long-term trend in the SSTs.

In addition to the above two warmer climate simulations, we carried out five additional simulations to assess the impact of the internal variability of the SPEAR LE. We divided the 30-member SPEAR LE into five groups, each containing six members, based on their performance in simulating the observed Pacific equatorial zonal east-west SST gradient, as defined above. These groups are referred to as SPEAR A, B, C, D, and E, with A denoting the best-performing and E the worst-performing group. Similar to the SPEAR ensemble mean (i.e., SPEAR-pattern M), SST anomalies for each group are derived based on their simulated trends from 1979–2020, averaged within each group. These simulations are referred to as SPEAR-patterns A, B, C, D, and E. To explore the impact of the various differences in SST trend patterns between the SPEAR ensemble mean (SPEAR-pattern M) and the observation (observed-pattern), we conducted four more simulations. These simulations mirror SPEAR-pattern M, except for replacing the SST anomalies in the Equatorial Pacific (110°–280°E, 10°S–10°N), the IPWP (50°–180°E, 30°S–30°N), the SO (0°–360°E, 45°–75°S), and the Atlantic tropical cyclone Main Development Region (275°–340°E, 10–25°N) with those from the observed-pattern. We applied a 3-grid-point running average five times along the edges (5 grid points) of each region to smooth the transition in SST anomalies between the region and the surrounding oceans. These simulations are denoted as SPEAR-patterns EPAC_{obs}, IPWP_{obs}, SO_{obs}, and AMDR_{obs}, respectively. They are used to assess how each of the regional differences in SST trends may affect the model-simulated high-impact

storm statistics, as well as hydrological and climate sensitivity. Similar to the observed-pattern simulation, the SST anomalies for each of the additional SPEAR-pattern simulations are rescaled by multiplying them by a constant so that the global open ocean mean SST anomaly matches that of SPEAR-pattern M (0.92 K). Note that this rescaling can slightly modify the SST anomalies outside of the replaced region for SPEAR-patterns EPAC_{obs}, IPWP_{obs}, SO_{obs}, and AMDR_{obs}. But the effect is very small. Finally, for all simulations (one control and 11 warmer climate simulations), the model was integrated for 101 years, with the last 100 years being used for analysis. These extended simulations are essential for studying the extreme high-impact storms.

Detection of AR, TS, and MCS days

The AR detection method is identical to the one used in refs. 17,19,48. The algorithm employed 6-hourly outputs of zonal and meridional vertically integrated vapor transport (IVT). It does not track individual ARs over time, so each IVT map is treated independently. The AR detection algorithm provides the 6-hourly output of AR objects, along with some basic measurements of each detected AR such as length, width, mean zonal and meridional IVT, and the coherence of IVT direction. These AR objects are used to identify grid cells experiencing AR conditions, which are further utilized to determine the AR days.

The TS detection method follows that used in refs. 49,50. In summary, we first identify potential cyclones by locating local maxima of relative vorticity exceeding a threshold value ($3.5 \times 10^{-5} \text{ s}^{-1}$). Subsequently, we define the nearby local minima of sea level pressure as cyclone centers using 6-hourly instantaneous fields of 850-hPa relative vorticity and sea level pressure. We then track individual tropical cyclones (TC) using their 6-hourly locations. The latitude of the first point (genesis location) of a TC track must be within [30°S–30°N]. After identifying a TC track, it is categorized as a TS if it satisfies all of the following three criteria for at least three days (not necessarily consecutive). (1) The maximum surface wind speed $\geq 17 \text{ m s}^{-1}$. (2) The maximum 850-hPa relative vorticity $\geq 1.6 \times 10^{-4} \text{ s}^{-1}$. (3) The warm-core temperature anomaly $\geq 2 \text{ K}$. We assume the $10^\circ \times 10^\circ$ (lat x lon) region centered at each TS's center location as the area experiencing a TS condition.

The MCS detection method follows the approach used in refs. 18,51, with some modifications described in ref. 19. To give a brief summary, the brightness temperature T_b is derived from the TOA outgoing longwave radiation (OLR) based on the equations in ref. 52. The algorithm then thresholds each 6-hourly instantaneous field of T_b by removing any grid cells with T_b values greater than 233 K^{18,51}. Because the spatial (temporal) resolution of the data [i.e., $0.5^\circ \times 0.625^\circ$ (lat x lon) and 6-hourly] is already larger (longer) than the smallest (shortest) MCSs, we do not further apply a size (duration) threshold for MCSs and simply consider any grid cells whose T_b values are below this threshold as regions experiencing MCS conditions¹⁹. As described in ref. 19, to detect MCSs in middle or high latitudes, we include an additional criterion by removing any grid cells whose T_b values are not 30 K smaller than the zonal mean values of the climatological T_b at the same latitude and same time of year. The climatological T_b is computed by taking a long-term (100-year) average of the 6-hourly T_b field at each location and time of year. This additional criterion has little impact over the tropics because the tropical zonal mean values of climatological T_b are always at least 30 K greater than 233 K. We consider any grid cells whose T_b values satisfy the above two criteria as regions in MCS conditions.

Finally, following ref. 19, for any given grid cells, if at least one AR/TS/MCS condition is identified from the 6-hourly data during a calendar day and the daily surface precipitation rate $P_{day} \geq 1 \text{ mm day}^{-1}$, the day is subsequently identified as an AR/TS/MCS day. We make AR, TS, and MCS days mutually exclusive by setting a priority for each identified phenomena. In particular, for any given grid cells, if a day satisfies multiple conditions, it is first considered as a TS day, then an AR day, and finally a MCS day. This priority choice is partly due to our confidence level for detecting TS, AR, and MCS days. Among the three phenomena, we have a relatively lower confidence for detecting MCS, thus we

consider a day as a MCS day only when it is neither an AR or a TS day. Using this classification, we conditionally sample the daily precipitation to explore the contribution of each storm regime to global and regional changes in precipitation.

Data availability

The Hadley Centre Sea Ice and Sea Surface Temperature data set (HadISST) is available at <https://www.metoffice.gov.uk/hadobs/hadisst/>. The NOAA Extended Reconstructed SST Version 5 data set (ERSSTv5) is available at <https://psl.noaa.gov/data/gridded/data.noaa.ersst.v5.html>. The COBE SST data set is available at <https://psl.noaa.gov/data/gridded/data.cobe.html>. The COBE2 SST data set is available at <https://psl.noaa.gov/data/gridded/data.cobe2.html>. The GFDL SPEAR Large Ensemble model outputs are publicly available at <https://noaa-gfdl-spear-large-ensembles-pds.s3.amazonaws.com/index.html#SPEAR/GFDL-LARGE-ENSEMBLES/CMIP/NOAA-GFDL/GFDL-SPEAR-MED/>. The model experiments that support the findings of this study, as well as the results of the control and future warmer climate simulations, are available from the corresponding author upon request.

Code availability

The GFDL AM4 model code used in this study is publicly available from <http://data1.gfdl.noaa.gov/nomads/forms/am4.0/>.

Received: 4 February 2024; Accepted: 1 June 2024;

Published online: 13 June 2024

References

- Wills, R. C. J., Dong, Y., Proistosescu, C., Armour, K. C. & Battisti, D. S. Systematic climate model biases in the large-scale patterns of recent sea-surface temperature and sea-level pressure change. *Geophys. Res. Lett.* **49**, e2022GL100011 (2022).
- Seager, R. et al. Strengthening tropical pacific zonal sea surface temperature gradient consistent with rising greenhouse gases. *Nat. Clim. Change* **9**, 517–522 (2019).
- Seager, R., Henderson, N. & Cane, M. Persistent discrepancies between observed and modeled trends in the tropical pacific ocean. *J. Clim.* **45**, 4571–4584 (2022).
- Heede, U. K., Fedorov, A. V. & Burls, N. J. Time scales and mechanisms for the tropical pacific response to global warming: a tug of war between the ocean thermostat and weaker walker. *J. Clim.* **33**, 6101–6118 (2020).
- Haumann, F. A., Gruber, N. & Münnich, M. Sea-ice induced southern ocean subsurface warming and surface cooling in a warming climate. *AGU Adv.* **1**, e2019AV000132 (2020).
- Dong, Y., Pauling, A. G., Sadai, S. & Armour, K. C. Antarctic ice-sheet meltwater reduces transient warming and climate sensitivity through the sea-surface temperature pattern effect. *Geophys. Res. Lett.* **49**, e2022GL101249 (2022).
- Dong, Y., Polvani, L. M. & Bonan, D. B. Recent multi-decadal southern ocean surface cooling unlikely caused by southern annular mode trends. *Geophys. Res. Lett.* **50**, e2023GL106142 (2023).
- Kang, S. M., Shin, Y., Kim, H., Xie, S.-P. & Hu, S. Disentangling the mechanisms of equatorial pacific climate change. *Sci. Adv.* **9**, eadf5059 (2023).
- Roach, L. A. et al. Winds and meltwater together lead to southern ocean surface cooling and sea ice expansion. *Geophys. Res. Lett.* **50**, e2023GL105948 (2023).
- Rugenstein, M., Dhame, S., Olonscheck, D., R. J. Wills, M. W. & Seager, R. Connecting the SST pattern problem and the hot model problem. *Geophys. Res. Lett.* **50**, e2023GL105488 (2023).
- Delworth, T. L. et al. SPEAR - the next generation GFDL modeling system for seasonal to multidecadal prediction and projection. *J. Adv. Model. Earth Syst.* **12**, e2019MS001895 (2020).
- Armour, K. C., Bitz, C. M. & Roe, G. H. Time-varying climate sensitivity from regional feedbacks. *J. Clim.* **26**, 4518–4534 (2013).
- Stevens, B., Sherwood, S. C., Bony, S. & Webb, M. J. Prospects for narrowing bounds on Earth's equilibrium climate sensitivity. *Earth's Future* **4**, 512–522 (2016).
- Gregory, J. M. & Andrews, T. Variation in climate sensitivity and feedback parameters during the historical period. *Geophys. Res. Lett.* **43**, 3911–3920 (2016).
- Zhao, M. An investigation of the effective climate sensitivity in GFDL's new climate models CM4.0 and SPEAR. *J. Clim.* **35**, 479–497 (2022).
- Rugenstein, M., Zelinka, M., Karnauskas, K. B., Ceppi, P. & Andrews, T. Patterns of surface warming matter for climate sensitivity. *EOS* **104**, e2023EO230411 (2023).
- Zhao, M. Simulations of atmospheric rivers, their variability, and response to global warming using GFDL's new high-resolution general circulation model. *J. Clim.* **33**, 10287–10303 (2020).
- Dong, W., Zhao, M., Ming, Y. & Ramaswamy, V. Representation of tropical mesoscale convective systems in a general circulation model: climatology and response to global warming. *J. Clim.* **34**, 5657–5671 (2021).
- Zhao, M. A study of AR-, TS-, and MCS-associated precipitation and extreme precipitation in present and warmer climates. *J. Clim.* **35**, 479–497 (2022).
- Dong, W., Zhao, M., Ming, Y., Krasting, J. P. & Ramaswamy, V. Simulation of United States mesoscale convective systems using GFDL's new high-resolution general circulation model. *J. Clim.* **36**, 6967–6990 (2023).
- Held, I. M. & Soden, B. J. Robust responses of the hydrological cycle to global warming. *J. Clim.* **19**, 5686–5699 (2006).
- Bretherton, C. S. & Smolarkiewicz, P. K. Gravity waves, compensating subsidence and detrainment around cumulus clouds. *J. Atmos. Sci.* **46**, 740–759 (1989).
- Bretherton, C. S. Insights into low-latitude cloud feedbacks from high-resolution models. *Phil. Trans. R. Soc. A* **373**, 20140415 (2015).
- Wood, R. & Bretherton, C. S. On the relationship between stratiform low cloud cover and lower-tropospheric stability. *J. Clim.* **19**, 6425–6432 (2006).
- Klein, S. A. & Hartmann, D. L. The seasonal cycle of low stratiform clouds. *J. Clim.* **6**, 1587–1606 (1993).
- Sobel, A. et al. Near-term tropical cyclone risk and coupled Earth system model biases. *Proc. Natl Acad. Sci.* **120**, e2209631120 (2023).
- Allen, M. R. & Ingram, W. J. Constraints on future changes in climate and the hydrologic cycle. *Nature* **419**, 224–232 (2002).
- Wentz, F., Ricciardulli, L., Hilburn, K. & Mears, C. How much more rain will global warming bring? *Science* **317**, 233–235 (2007).
- Otto, A. et al. Energy budget constraints on climate response. *Nat. Geosci.* **6**, 415–416 (2013).
- Mauritsen, T. & Stevens, B. Missing iris effect as a possible cause of muted hydrological change and high climate sensitivity in models. *Nat. Geosci.* **8**, 346–351 (2015).
- Lindzen, R. S., Chou, M. & Hou, A. U. Does the earth have an adaptive infrared iris? *Bull. Amer. Meteor. Soc.* **82**, 417–432 (2001).
- Zhou, C., Zelinka, M. D. & Klein, S. A. Analyzing the dependence of global cloud feedback on the spatial pattern of sea surface temperature change with a green's function approach. *J. Adv. Model. Earth Syst.* **9**, 2174–2189 (2017).
- Dong, Y., Proistosescu, C., Armour, K. C. & Battisti, D. S. Attributing historical and future evolution of radiative feedbacks to regional warming patterns using a green's function approach: the preeminence of the western pacific. *J. Clim.* **32**, 5471–5491 (2019).
- Zhang, B., Zhao, M. & Tan, Z. Using a green's function approach to diagnose the pattern effect in gfdl am4 and cm4. *J. Clim.* **36**, 1105–1124 (2023).

35. Zhang, S., Stier, P., Dagan, G., Zhou, C. & Wang, M. Sea surface warming patterns drive hydrological sensitivity uncertainties. *Nat. Clim. Change* **13**, 545–553 (2023).
36. Zhang, B. et al. The dependence of climate sensitivity on the meridional distribution of radiative forcing. *Geophys. Res. Lett.* **50**, e2023GL105492 (2023).
37. Bloch-Johnson, J. et al. The Green's function model intercomparison project (GFMIP) protocol. *J. Adv. Model. Earth Syst.* **16**, e2023MS003700 (2024).
38. Alessi, M. & Rugenstein, M. Surface temperature pattern scenarios suggest higher warming rates than current projections. *Geophys. Res. Lett.* **50**, e2023GL105795 (2023).
39. Watanabe, M., Dufresne, J.-L., Kosaka, Y., Mauritsen, T. & Tatebe, H. Enhanced warming constrained by past trends in equatorial Pacific sea surface temperature. *Nat. Clim. Change* **11**, 33–37 (2021).
40. Kim, H., Kang, S. M., Kay, J. E. & Xie, S.-P. Subtropical clouds key to southern ocean teleconnections to the tropical Pacific. *Proc. Natl Acad. Sci.* **119**, e2200514119 (2022).
41. Kang, S. M. et al. Global impacts of recent southern ocean cooling. *Proc. Natl Acad. Sci.* **120**, e2300881120 (2023).
42. Wang, B. et al. Understanding the recent increase in multiyear La Niñas. *Nat. Clim. Change* **13**, 1075–1081 (2023).
43. Zhao, M. et al. The GFDL global atmosphere and land model AM4.0/LM4.0 – Part I: simulation characteristics with prescribed SSTs. *J. Adv. Model. Earth Syst.* **10**, 691–734 (2018).
44. Zhao, M. et al. The GFDL global atmosphere and land model AM4.0/LM4.0 – Part II: model description, sensitivity studies, and tuning strategies. *J. Adv. Model. Earth Syst.* **10**, 735–769 (2018).
45. Haarsma, R. J. et al. High resolution model intercomparison project (HighResMIP v1.0) for CMIP6. *Geosci. Model Dev.* **9**, 4185–4208 (2016).
46. Murakami, H. et al. Detected climatic change in global distribution of tropical cyclones. *Proc. Natl. Acad. Sci.* **117**, 10706–10714 (2020).
47. Adcroft, A. et al. The GFDL global ocean and sea ice model OM4.0: model description and simulation features. *J. Adv. Model. Earth Syst.* **11**, 3167–3211 (2019).
48. Guan, B. & Waliser, D. E. Detection of atmospheric rivers: evaluation and application of an algorithm for global studies. *J. Geophys. Res.* **120**, 12514–12535 (2015).
49. Zhao, M., Held, I. M., Lin, S.-J. & Vecchi, G. A. Simulations of global hurricane climatology, interannual variability, and response to global warming using a 50 km resolution GCM. *J. Clim.* **22**, 6653–6678 (2009).
50. Zhao, M., Held, I. M. & Lin, S.-J. Some counterintuitive dependencies of tropical cyclone frequency on parameters in a GCM. *J. Atmos. Sci.* **69**, 2272–2283 (2012).
51. Huang, X. M. et al. A long-term tropical mesoscale convective systems dataset based on a novel objective automatic tracking algorithm. *Clim. Dyn.* **51**, 3145–3159 (2018).
52. Ellingson, R. G. & Ferraro, R. R. An examination of a technique for estimating the longwave radiation budget from satellite radiance observations. *J. Clim. Appl. Meteorol.* **22**, 1416–1423 (1983).

Acknowledgements

We thank Drs. Isaac Held, Zhihong Tan, and Leo Donner for their comments and suggestions. The statements, findings, conclusions, and recommendations are those of the authors and do not necessarily reflect the views of the National Oceanic and Atmospheric Administration or the US Department of Commerce.

Author contributions

M.Z. designed and performed research; M.Z. analyzed data; M.Z. and T.K. wrote the paper.

Competing interests

The author declares no competing interests.

Additional information

Supplementary information The online version contains supplementary material available at <https://doi.org/10.1038/s41612-024-00681-7>.

Correspondence and requests for materials should be addressed to Ming Zhao.

Reprints and permissions information is available at <http://www.nature.com/reprints>

Publisher's note Springer Nature remains neutral with regard to jurisdictional claims in published maps and institutional affiliations.

Open Access This article is licensed under a Creative Commons Attribution 4.0 International License, which permits use, sharing, adaptation, distribution and reproduction in any medium or format, as long as you give appropriate credit to the original author(s) and the source, provide a link to the Creative Commons licence, and indicate if changes were made. The images or other third party material in this article are included in the article's Creative Commons licence, unless indicated otherwise in a credit line to the material. If material is not included in the article's Creative Commons licence and your intended use is not permitted by statutory regulation or exceeds the permitted use, you will need to obtain permission directly from the copyright holder. To view a copy of this licence, visit <http://creativecommons.org/licenses/by/4.0/>.

This is a U.S. Government work and not under copyright protection in the US; foreign copyright protection may apply 2024